

WFC3/UVIS Encircled Energy

J. Medina, J. Mack & A. Calamida
March 18, 2022

ABSTRACT

We compute new UVIS encircled energy (EE) curves from images of HST standard stars observed from 2009-2020, after correcting for temporal changes in the sensitivity of each CCD and filter. The latest UVIS photometric calibration (Calamida et al. 2021) makes use of the updated EE values presented in this report for two filters (F275W and F814W). We extend this analysis to five additional filters (F336W, F200LP, F350LP, F775W, and F850LP) to investigate differences between the 2009 EE, derived just after WFC3's installation, and the 2016 chip-dependent EE, computed by averaging inflight observations over ~6 years. To recompute the EE, we rescale the calibrated FLC science array values using the new time-dependent inverse sensitivity (PHOTFLAM) keyword values, align the images in detector coordinates, and combine all images in a given CCD and filter. This process allows for a more accurate measure of the PSF at large radii out to 6 arcsec. We compare the EE values in a 10-pixel radius aperture, EE(10), used for the photometric calibration, and we find that the values for the two CCDs now agree to ~0.1% for each filter, compared to the 2016 solutions which differed by up to 0.5%. At UV wavelengths, the EE(10) is now lower by ~1% for both CCDs, in closer agreement with the 2009 solution. For two 'red' filters (F775W and F850LP), we compare the EE curves for a white dwarf and a G-type star but find no significant differences due to the color of the source. The new EE(10) values will be applied in a future update to the UVIS photometric calibration.

1. Introduction

The WFC3/UVIS photometric calibration is derived from aperture photometry of HST standard stars measured in a radius of 10-pixels and then corrected to 'infinity' (150 pixels) using the encircled energies (EEs). The first in-flight EE estimates were based on observations of GD153 in the F275W and F625W filters, with exposure times ranging from 10 to 800 seconds via program CAL/WFC3 11438 (Hartig 2009). These data were combined by successively replacing saturated pixels and their immediate neighbors with values from the next shorter exposure, scaled by their

relative exposure time, to produce a high-dynamic-range image for each filter. This allowed for measurement of the Point Spread Function (PSF) wings out to radius of ~ 6 arcsec (150 pixels) via the azimuthally-averaged fractional flux per pixel. To extrapolate the observed data to other wavelengths, the authors derived a wavelength-dependent EE model using the measured PSFs, the OTA (Optical Telescope Assembly) pupil geometry, the OTA mirror mid-frequency optical path difference maps, and an estimate of the detector blur.

In 2016, new chip-dependent EE curves were computed for all 42 full frame filters. These were based on observations of HST’s three primary CALSPEC white dwarf (WD) standards (GD153, G191B2B, and GD71) acquired in the WFC3 Photometry Monitor and spanning a period of ~ 6 years (Deustua et al. 2016). The chip-dependent approach was adopted to account for the different quantum efficiencies of the two UVIS CCDs (chips) and evidence that the two CCDs were aging differently. The updated EE solutions were derived for each CCD from drizzle-combined images of each standard star averaged over WFC3’s lifetime.

Temporal changes in the detector sensitivity were first reported by Gosmeyer et al. (2014) based on images from the UVIS Contamination Monitor, which observed the WD standard GRW+70d5824 (hereafter GRW+70) every ~ 6 weeks in several key filters. Shanahan et al. (2017) extended these results using three additional years of GRW70 images plus observations of second WD standard, GD153. The later star was observed regularly in the first few cycles of the Contamination Monitor and then reduced to a less frequent cadence of 1-2 times per year via the Photometry Monitor. In late-2016 (Cycle 24), the Contamination Monitor resumed more regular observations of GD153 after GRW+70 was suspected to be variable at a 2-sigma level (Bohlin & Landolt 2015).

Khandrika et al. (2018) extended the investigation of temporal changes to larger number of UVIS filters but limited the data sample to the three primary WDs plus the CALSPEC G-type standard P330E observed in the Photometry Monitor. The authors reported changes in the observed photometry of $\sim 0.1\%$ to 0.3% per year, similar to prior studies which included GRW+70.

In late-2017, the CALSPEC spectrum of GRW+70 was updated to incorporate new STIS observations in the G430L and G750L region (CAL/WFC3 14871). With the improved wavelength coverage and the multitude of UV observations for monitoring the changing STIS sensitivity, the observed spectrum of GRW+70 ‘*grw_70d5824_stiswfcnic_002.fits*’ was upgraded to being considered ‘one of the best (secondary) CALSPEC standards’ (Bohlin et al. 2020), after the three primary WDs. Furthermore, routine monitoring of this star with STIS, ACS & WFC3 showed similar time-dependent changes as measured for the three primary WDs, with no suggestion of systematic variability to within a limit of $\sim 1\%$ (Bohlin 2022, private communication).

By 2020, the observed countrates in the popular F606W filter were $\sim 2\%$ lower than for images acquired in 2009. Using observations of all five CALSPEC standards, Calamida et al. (2021) recomputed temporal changes in the sensitivity for the two CCDs. Because GRW+70 was observed at a more regular cadence than the other HST standards, including this standard in the analysis has the effect of reducing the error in the computed slopes (observed count rate versus time) derived from linear fitting, compared to the less frequently sampled stars from the Photometry Monitor. These results were used to update the UVIS photometric calibration with a

new set of time-dependent inverse sensitivity (PHOTFLAM) values. The new solutions were delivered to the Calibration Database Reference System (CRDS) in October 2020 for use in **calwf3** to produce calibrated data products for download from MAST.

With the exception of a few filters, Calamida et al. (2021) used the 2016 EE(10) values to correct aperture photometry in a 10 pixel radius, but these did not account for temporal changes and therefore carried small systematic errors. For the F275W and F814W filters, however, EE curves were recomputed for each CCD based on hundreds of images of GRW+70 acquired over WFC3’s lifetime. In their report, Calamida et al. (2021) highlight the new techniques for computing EE curves which are described in more detail in this report. These include: 1.) correcting the image science arrays for changes in the observed count rates, 2.) aligning the images in detector coordinates (not in sky coordinates), and 3.) combining the images with **AstroDrizzle** to produce high signal-to-noise PSFs at large radii.

While the 2009 EE(10) values were derived from deep exposures in F275W, the EE(10) values from 2016 chip-dependent solutions were $\sim 1\%$ different than expectations. Calamida et al. (2021) showed that correcting for time-dependence brings the EE(10) values to closer agreement to the 2009 value. Additionally, the 2016 EE(10) values were different by $\sim 0.5\%$ across the two CCDs for several filters. To check this discrepancy, images in the F814W filter were reprocessed with time-dependent corrections, and the differences between the two CCD disappeared. In this work, we extend our analysis to include the F336W and F775W filters to test whether the differences in 2016 EE across chips are a result of systematic errors introduced by the changing sensitivity.

For filters with very few calibration images, Calamida et al. (2021) predicted that the 2016 EE(10) values may have very large uncertainties which could explain their low values compared to the 2009 model predictions. For example, the F200LP chip-dependent EE(10) is $\sim 4\%$ smaller than the 2009 value, and the F850LP EE(10) values is $\sim 2\%$ larger. We rederive EE curves for these two filters using a larger set of on-orbit images, and we add F350LP to our sample, which is $\sim 1\%$ lower in the chip-dependent solution compared to the optical model near 6000 Å.

In this report, we describe the observations used for recomputing the EE curves in Section 2, and we provide details on the data reduction techniques in Section 3. We show examples of the drizzle-combined PSFs, the radial profiles, and the EE fraction as a function of aperture radius in Section 4. We summarize our findings in Section 5, where we compare our results with prior solutions, and we highlight our conclusions in Section 6. In the Appendix, we provide EE plots for each standard star in a given CCD and filter.

2. Observations

Several WFC3 calibration programs regularly monitor one or more HST CALSPEC standard stars: the white dwarfs GD153, GD71, G191B2B, and GRW+70, and the G-type star P330E. For this work, we used observations from the ‘WFC3 Photometry Monitor’ and the ‘UVIS Contamination Monitor’ acquired between 2009 and 2020 (see Table 1). For the analysis, we downloaded the calibrated, CTE-corrected images from MAST which were processed with **calwf3**. These are referred to hereafter as FLC frames and have the suffix ‘*_flc.fits*’.

When planning the observations, exposure times for each CCD and filter were chosen to provide high signal to noise ratios, SNRs = 100-1000, within the standard UVIS aperture radius of 10 pixels (0.396 arcsec). To mitigate the growing CTE losses over time, observations after Cycle 20 were acquired with a post-flash level of 12 electrons, while observations after Cycle 28 were acquired with a larger recommended post-flash level of 20 electrons. For each visit, observations within a given filter consist of either a 2-point line dither pattern, a 4-point box dither, or a combination of line and box dithers. This allows for the removal of detector artifacts and cosmic rays when combining frames. Dither offsets are in non-integer pixels so that the star is not centered within a pixel for at least one position, which helps mitigate saturation.

The Photometry Monitor routinely samples all four corners of the UVIS detector via the standard 512 x 512 subarrays, while the Contamination Monitor samples only the UVIS1-C512A and UVIS2-C512C corner subarrays. Because observations from each chip are combined to produce a deep image of each target, the UVIS1-C512B and UVIS2-C512D subarray images were not used in order to avoid introducing systematic errors due to uncertainties in the flat field calibration (e.g. see Mack et al. 2016, Khandrika et al. 2018).

Table 1: Calibration programs (CAL/WFC3) used to recompute the encircled energies.

Program	Program IDs
WFC3 Photometry Monitor	11450, 11903, 13089, 13575, 14021, 14384, 14883, 14992, 15399, 15582, 16030, 16415
UVIS Contamination Monitor	11426, 11907, 12333, 12698, 13088, 13574, 14018, 14382, 14815, 14878, 15398, 15583

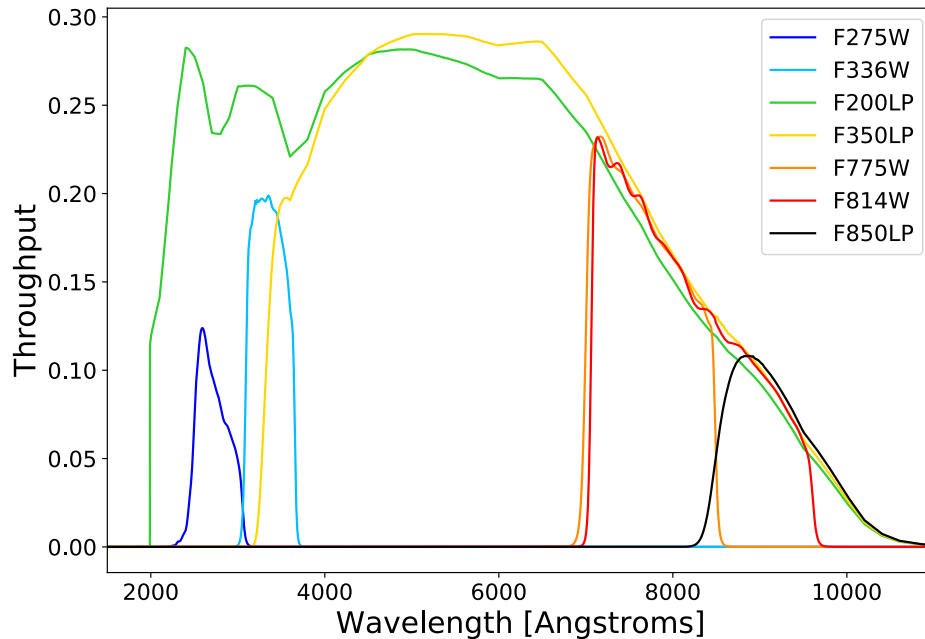


Figure 1: UVIS1 total system throughput for the seven wide and long-pass filters in this study.

To recompute the EE, we selected CALSPEC standards with the largest number of observations in each of the seven filters, GD153, GRW+70, and P330E. We chose the G-type star P330E to investigate any effect of spectral type on the EE curves for red filters. This check was not performed for blue filters due to a limited set of calibration observations of P330E at shorter wavelengths. The throughput curves for the filters in this study are plotted in Figure 1 and span the entire spectral range of the UVIS1 detector. Throughput curves for the UVIS2 detector may be found in Appendix A.2 of the WFC3 Instrument Handbook (Dressel et al. 2022). The rms bandwidth and the pivot wavelength for each filter are reported in Table 3.

3. Analysis

Relative photometry (the percent change in the observed count rate) of GRW+70 is shown in Figure 2 as a function of observation date (in Modified Julian Date, MJD) for the F814W filter measured on the UVIS2 CCD in the Amplifier (Amp) C subarray. Light grey points highlight aperture photometry ($r=10$ pixels) on single calibrated, CTE-corrected FLC images and span a total range of ~ 10 years. Black circles show relative photometry of drizzled (DRC) images, derived from combining sets of FLC frames in ~ 140 day bins with no time-dependent corrections. These DRC images have improved SNR and have been corrected for both bad pixels and cosmic-rays. While the scatter in the (fewer) DRC points is much less than the scatter in the (more numerous) FLC points, the slopes derived from each, DRC versus FLC, typically agree to within $\sim 0.01\%$ per year for most filters.

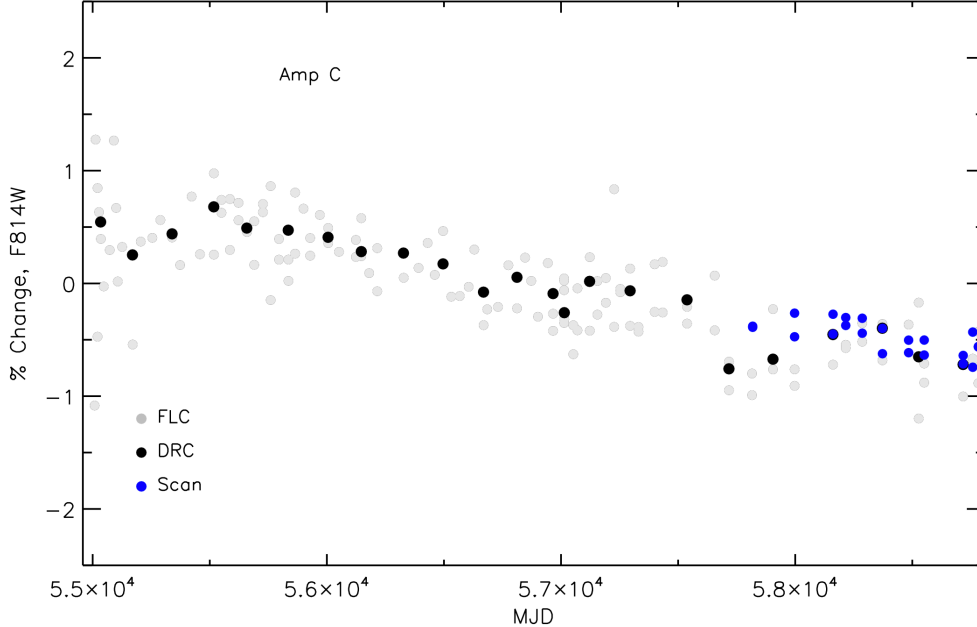


Figure 2: Percent change in the observed count rate of GRW+70d5824 versus date (MJD) for UVIS2/F814W in the Amp C subarray. Grey circles show aperture photometry in a 10-pixel radius from calibrated (FLC) images, while black circles represent aperture photometry from drizzle-combined (DRC) images in bins of ~ 140 days. Relative photometry of spatially scanned observations are shown as blue circles for images acquired between 2017 and 2020. Scanned photometry shows a reduced scatter compared to the staring-mode (FLC or DRC) photometry.

Blue points in Figure 2 show relative photometry of spatially scanned observations of GRW+70 acquired via the ‘UVIS Contamination Monitor’ (Shanahan et al. 2017b, Calamida et al 2021). We note that scanned photometry has an even lower scatter than the DRC staring-mode photometry. Calamida et al. (2021) used both staring- and scanning-mode photometry to compute the linear fits for each CCD and filter using all five CALSPEC standards. The linear fit for F814W on UVIS2 is presented in Figure 6.21 of the WFC3 Instrument Handbook and shows a slow decline in the sensitivity of -0.11 percent per year. We used this slope value to correct the individual FLC observations of GRW+70 prior to combining the frames with **AstroDrizzle**.

In the following sections, we describe the steps used for recomputing the EE curves:

3.1 Scale the FLC’s

We begin by scaling the FLC images to correct for changes in the observed count rates. For data products acquired from MAST after October 2020, **calwf3** (v3.5.1 and higher) uses an updated UVIS image photometry table (IMPHTTAB) reference file (*‘51c1638pi imp.fits’*) to populate time-dependent photometry keywords in the headers of calibrated images. The blue datapoints in Figure 3 represent the PHOTFLAM values for UVIS2 populated in the IMPHTTAB at regular intervals in time, and these incorporate the slope of the linear fit to all five CALSPEC standards from Calamida et al. (2021). In pink, we overplot the interpolated (time-dependent) PHOTFLAM values corresponding to the individual observation dates (in MJD) for GRW+70.

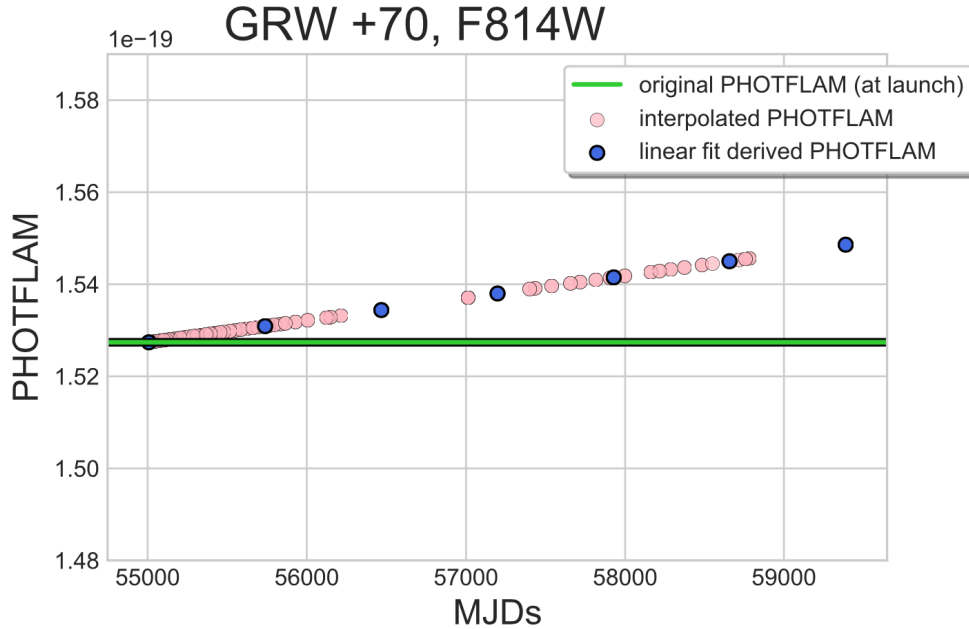


Figure 3: Time-dependent PHOTFLAM (inverse sensitivity) values from the IMPHTTAB (in units $1e-19 \text{ erg/s/cm}^2/\text{\AA}$ per *electron/sec*) are shown for UVIS2/F814W as a function of MJD (filled blue circles, spaced uniformly with time). The green horizontal line represents the PHTFLAM2 value at the UVIS ‘reference date’ (MJD=55008 or June 26, 2009). Pink circles show the ‘interpolated’ PHTFLAM2 values corresponding to the individual GRW+70 observations. The plot shows how the inverse sensitivity values increase over time as the detector sensitivity declines.

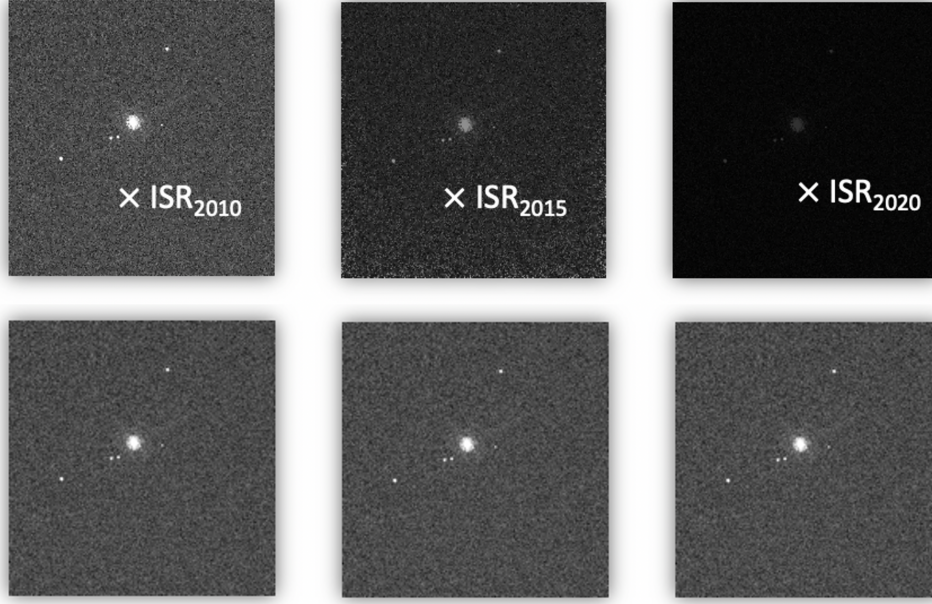


Figure 4: A visual representation of the sensitivity loss over time (top row) for three identical FLC images of GRW+70 (in *electrons*) observed in different years: 2010, 2015, 2020. Scale differences have been artificially enhanced for illustration. Each FLC is multiplied by its corresponding Inverse Sensitivity Ratio ($ISR_{DATE} = PHOTFLAM_{DATE} / PHOTFLAM_{2009}$) normalized to a reference date in 2009 (see text). This produces a set of modified FLC' images (bottom row) in which the star has roughly similar observed count rates. This step is required before drizzling the separate FLC frames to produce a high SNR composite image.

The individual FLC images were modified using the task **phot_eq** in **DrizzlePac** (<https://drizzlepac.readthedocs.io/en/latest/photeq.html>) which uses the PHOTFLAM values in the image header to correct the science array pixel values based on the ratio of the inverse sensitivity value of each image with respect to a reference date in 2009 (e.g. MJD=55008). Figure 4 is a visual representation of three FLC frames taken 5 years apart, where the observed count rates in the top row are decreasing over time. For illustration, the date in the figure is indicated in years, whereas the actual values correspond to the observation MJD, as given in the header keyword EXPSTART. In the bottom panel, the FLC science arrays have been scaled by the inverse sensitivity ratio, ISR_{MJD} , to produce a modified image FLC', with roughly equal count rates:

$$FLC' = FLC * ISR_{MJD} = FLC * \frac{PHOTFLAM_{MJD}}{PHOTFLAM_{55008}}$$

3.2 Align

The FLC images now have roughly equal count rates, which is required for optimal image combination with the **AstroDrizzle** software, also available in **DrizzlePac** (<https://drizzlepac.readthedocs.io/en/latest/astrodrizzle.html>). By combining many datasets, we significantly improve the signal-to-noise ratio standard star at large radii, enabling more accurate analysis of the PSF wings out to a radius of 150 pixels.

Whereas the drizzling algorithm uses World Coordinate System (WCS) information from the image header to align observations in sky coordinates, **we instead align the images in detector coordinates**. This ensures that the drizzled PSF does not rotate as the nominal HST orientation changes over the year, which changes the position of the diffraction spikes and structure in the PSF wings. This is done by modifying the following astrometry header keywords for each FLC:

1. The CRPIX1 and CRPIX2 values are modified to match the X,Y position of the star's centroid in each image in order to account for pointing errors;
2. The CRVAL1 and CRVAL2 are set to match the value of the reference (first) image in order to remove any proper motion applied to the RA and Dec of the star over ~ 10 years;
3. The linear terms of the CD matrix (CD1_1, CD1_2, CD2_1, CD2_2) are set to match the value from the reference (first) image in order to remove any orientation and plate scale changes with date.

3.3 Drizzle

Once the WCS keywords were updated, we combined the FLC images with **AstroDrizzle** using the parameters listed in Table 2, where only non-default values are listed. By aligning the star in detector space, we were able to accurately flag cosmic rays and detector artifacts (e.g. unstable hot pixels) while not affecting any PSF structure (e.g. diffraction spikes, Airy rings). Additionally, by not rotating the images on the sky, the FLC frames have minimal pixel resampling.

To verify the accuracy of the drizzled products, we examined the weight images (equivalent to an exposure time map) to verify that the core of the star was not improperly misidentified and flagged as a cosmic ray in any of the individual exposures. This would show up as a reduced total exposure time at the center of the star and typically compromises the accuracy of the stellar photometry.

Table 2: AstroDrizzle parameters with non-default settings used for this analysis.

Name	Description	Value
skymethod	Equalize sky background between the input frames	match
skystat	Use the sigma-clipped mean background	mean
driz_sep_bits	For single images, set DQ values considered to be good data	64, 16
combine_type	Combine images using the median	median
combine_nhigh	Number of high value pixels to reject for the median	1
driz_cr_snr	S/N to be used for detecting CRs, performed in two iterations	3.5 3.0
driz_cr_scale	Scaling factors applied to the derivative for detecting CRs	2.0 1.5
final_bits	For the final stack, set DQ values considered to be good data	64, 16

Next, we examined the drizzle-combined images for each CCD and filter, plotted the 1-dimensional radial profiles, and examined the PSF shape and FWHM values. The radial profile is also referred to as the ‘azimuthal average’ and represents the average pixel value in a 1-pixel wide ring moving radially outward from the centroid. These results are presented in Section 4.

3.4 Calculate Encircled Energies

Finally, we calculated the encircled energy or ‘curve of growth’ from the drizzled images for each star. Using the **Photutils** (<https://photutils.readthedocs.io>) photometry package, we computed the flux (in *electrons/sec*) for a range of circular apertures with radii varying from 1 pixel to 150 pixels (~ 6 arcsec). The largest 150-pixel aperture is defined as the UVIS ‘*infinite*’ aperture which encloses 100% of the light from a point source, and all other apertures were normalized to this radius.

The photometry in each aperture was then corrected by an estimate of the sky background per pixel, computed as the 3-sigma clipped mean value in an annulus extending from $r=160$ to 200 pixels. Factoring in small offsets in the star’s position (~ 5 -10 pixels) due to pointing errors, this outer radius rarely ever encroaches on the edges of the 512x512 corner subarray where the flat field is typically less accurate (see Mack et al. 2013).

4. Results

4.1 Radial Profiles

We show a zoomed region of the F814W drizzled image in Figure 6 for GRW+70 in Amp A on UVIS1 (top) and Amp C on UVIS2 (bottom), where the dashed circle is shown for scale and indicates a radius of 50 pixels. The diffraction spikes are rotated slightly from their nominal 45-degree position as a result of aligning the WCS solutions with respect to the first image in each set and then drizzling. This rotation does not affect the shape of the EE curves, which are 1-dimensional radial profiles.

The radial profiles for F814W are shown in Figure 7 for Amp A (top) and Amp C (bottom). The ‘bumps’ at radii 3, 8 and 12 pixels are due to the local maxima of the Airy rings surrounding the PSF. These bumps are slightly smoothed out in Amp A compared to Amp C. This can be attributed to the elongated shape of the PSF in the upper left corner of the detector where Amp A sits. In this corner, the PSF shape varies significantly with the changing focus (see Dressel, 2013; Sabbi & Bellini, 2013; Anderson et al., 2016).

The WFC3 Instrument Handbook gives the FWHM of the UVIS PSF at 8000 Å to be 1.84 pixels in native (FLC) pixels (Dressel et al. 2022, Table 6.7). A PSF measured in drizzled (DRC) pixels will have a slightly larger FWHM due to the convolution of the data with a ‘square’ drizzle kernel function, which used to distribute the flux onto the output pixel grid. We measure a FWHM in the F814W combined DRC frames of ~ 2.0 pixels for both CCDs, in agreement with expectations for a well-aligned stack of input frames.

Radial profiles for F850LP and F200LP in Amp C are highlighted in Figure 8. The top panel shows the combined GRW+70 observations in F850LP, while the bottom panel shows the combined P330E observations in F200LP. Airy rings in the narrower F850LP filter ($\Delta\lambda = 470 \text{ \AA}$) are even more distinct than in the very wide F814W filter ($\Delta\lambda = 670 \text{ \AA}$) and can be seen at radii of $\sim 3, 9, 15, 21$, and 27 pixels. These features are not visible at all in the widest F200LP filter ($\Delta\lambda = 1740 \text{ \AA}$), where the light is a combination of many overlapping wavelengths and these features cancel out.

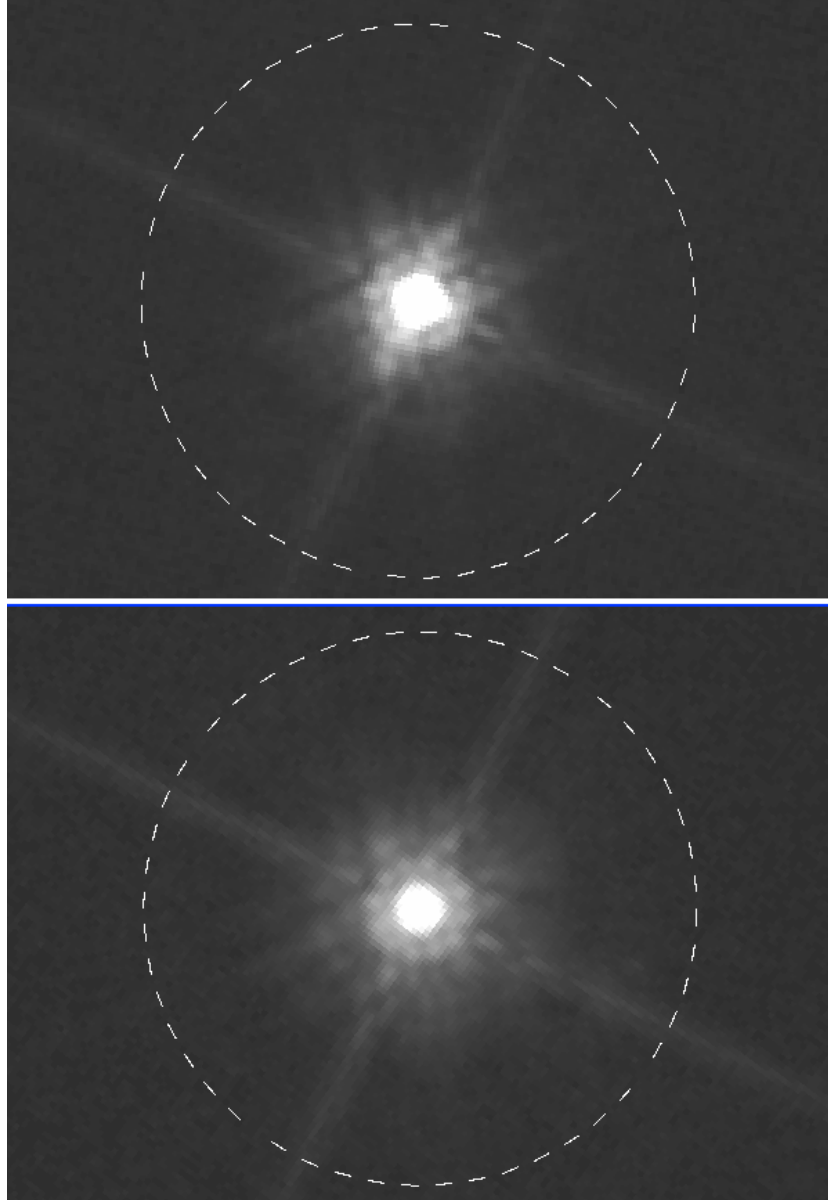


Figure 6: Drizzled images of GRW+70 in F814W observed in Amp A (top) and Amp C (bottom) with exposure times of ~ 1000 seconds each. A dashed circle with a radius of 50 pixels (2.0 arcsec) is shown for scale. The EE curves were computed with respect to an ‘*infinite*’ aperture radius of 150 pixels, but the figure is zoomed in to highlight structure in the inner PSF region. The diffraction spikes are rotated slightly as a result of aligning the WCS to the first image in each set.

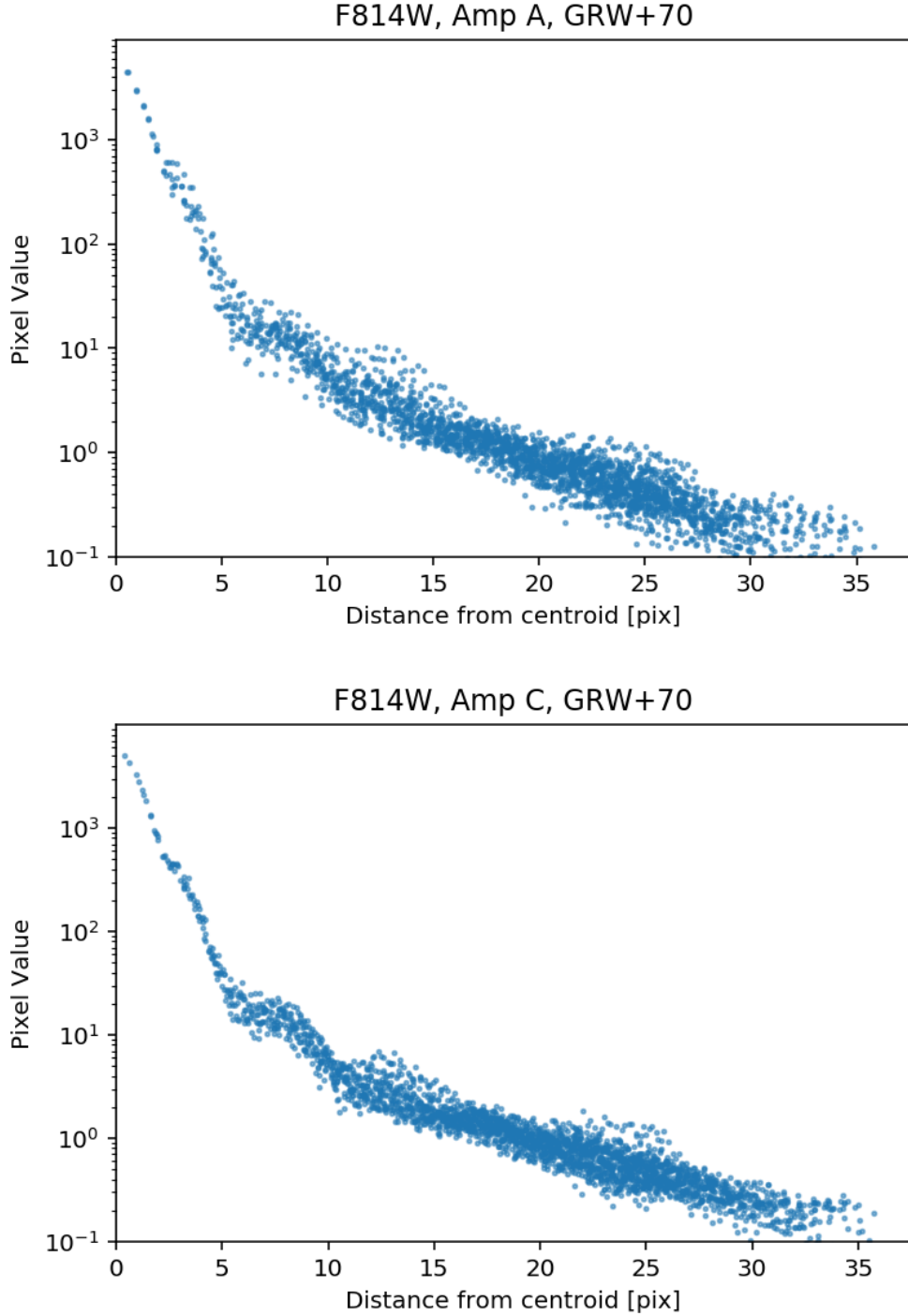


Figure 7: The radial profile of the drizzle-combined stack of GRW+70 images in F814W. This represents the average pixel value in a 1-pixel wide ring moving radially outward from the centroid. The ‘bumps’ at radii 3, 8 and 12 pixels are the Airy rings of the PSF. We attribute the slightly smoothed out ‘bumps’ in Amp A (top panel) to the elongated shape of the PSF in the upper left corner of UVIS1 which varies significantly from image to image. The PSF is much more stable in the lower left detector corner of UVIS2 where Amp C sits (bottom panel).

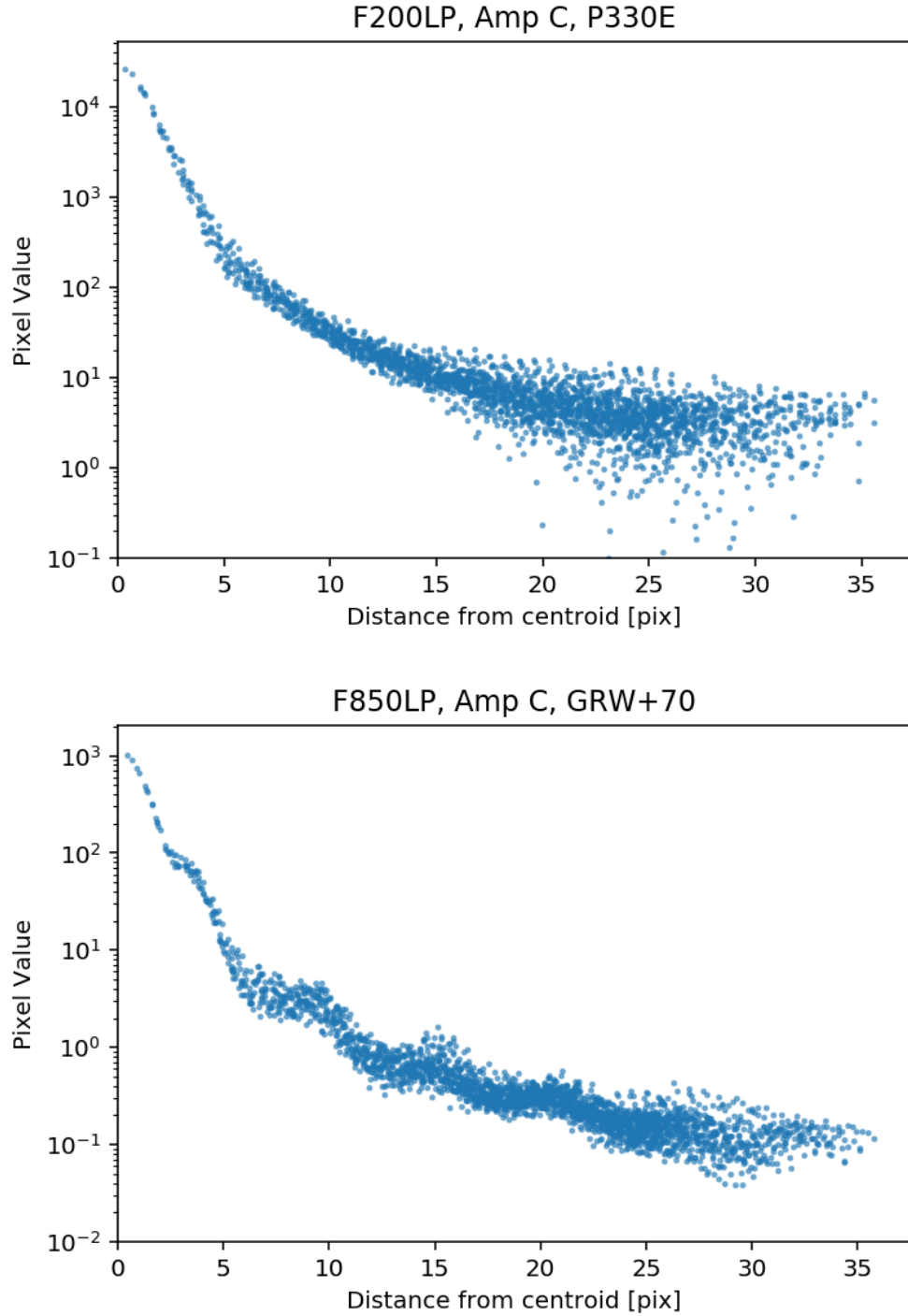


Figure 8: (Top) Radial profile of GRW+70 observed in the F850LP filter in Amp C. Airy rings can be seen at $r=3, 9, 15, 21,$ and 27 pixels. (Bottom) Radial profile of P330E observed in the F200LP filter. Airy rings are not apparent in this profile because of the very wide bandpass of the filter, so that the rings of various wavelengths do not constructively superpose but instead tend to cancel each other out.

4.2 EE Curves

EE curves from 10 to 150 pixels are shown in Figure 9 for Amp A, which typically has many more observations than the other amps. As in Figure 1, we color coded the seven filters from blue to red according to their respective pivot wavelength (λ_p), and we note an overall trend in the shape of the EE curves with wavelength. For radii < 28 pixels, the EE is lowest for blue filters and rises more steeply compared to redder filters. For radii > 40 pixels, the EE for blue filters then rises more slowly from 0.98 to 1.0 compared to redder filters where it rises from 0.97 to 1.0. One exception is the very red F850LP filter ($\lambda_p = 9200 \text{ \AA}$), where the EE is midway between F275W and F814W for radii < 28 pixels and then more closely tracks the F775W and F814W curves at larger radii.

These results are consistent with the EE plot in the WFC3 Instrument Handbook (Dressel et al. 2022, Figure 6.15) which shows the 2009 UVIS EE model at 200, 400, and 800 nm. In that plot, 200 and 800 nm curves cross at a radius of $0.9''$ (23 pixels), where they enclose $\sim 95\%$ of the light. In Figure 9 of this report, the F275W and F814W EE curves cross at a radius of $\sim 1.1''$ (28 pixels),

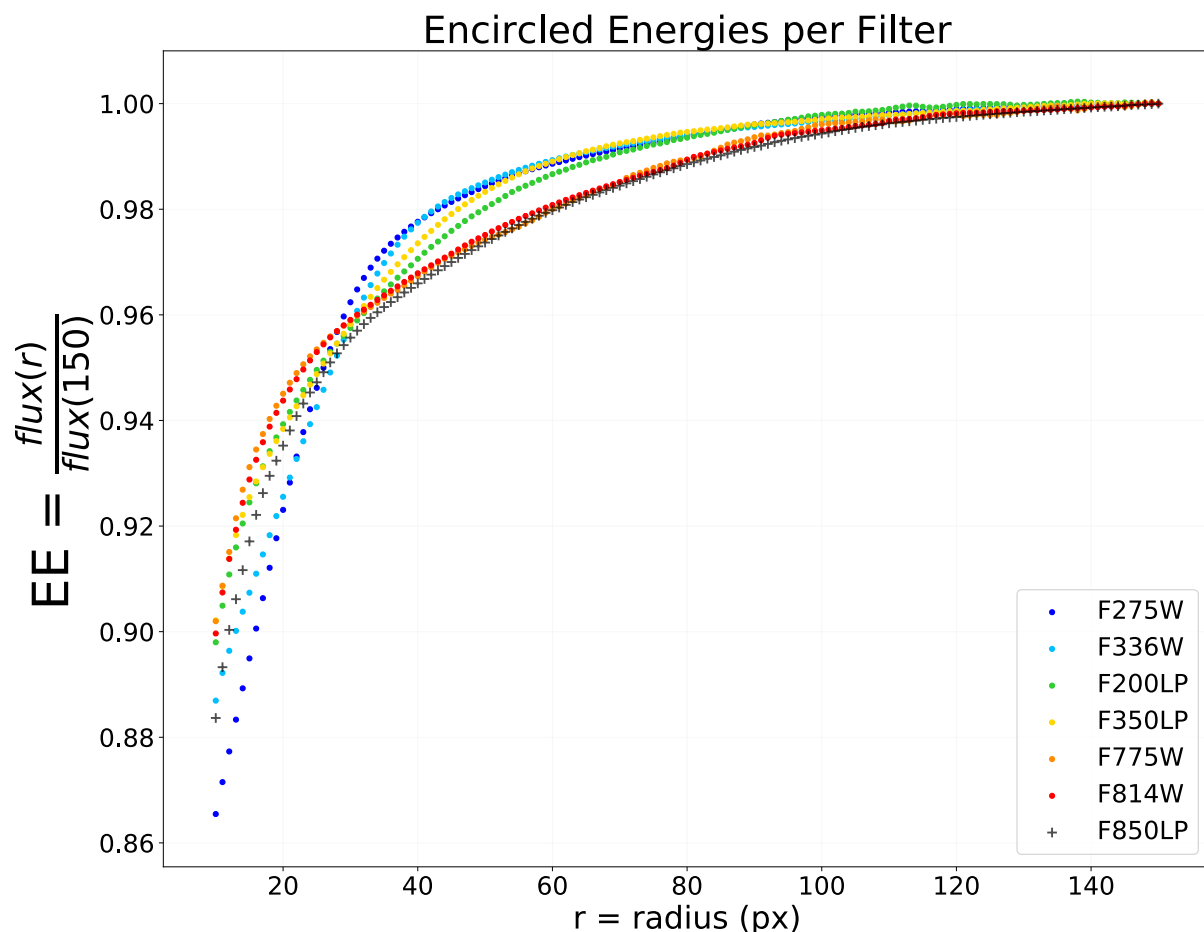


Figure 9: UVIS1 (Amp A) Encircled Energy versus radius for seven filters sampling a large range of detector wavelengths. The EE values are normalized to the flux (count rate) at 150 pixels and are based on deep stacks of drizzle-combined images of **GRW+70** (F275W, F336W, F814W, and F850LP), **GD153** (F350LP and F775W), and **P330E** (F200LP) from calibration monitoring.

where they enclose $\sim 96\%$ of the light. We suspect that these small differences are due to uncertainties in the 2009 solution at 800 nm, which was based on deep F275W and F625W images plus an optical model to extrapolate to longer wavelengths.

4.3 EE at 10 Pixels

The chip-dependent EE evaluated at an aperture radius of 10 pixels is equal to the ratio of the flux at 10 pixels and the flux at 150 pixels, e.g. $EE(10) = flux_{10} / flux_{150}$. This quantity is plotted as a function of the filter pivot wavelength in Figure 10 and is used as part of the UVIS photometric calibration to correct aperture photometry of CALSPEC standards measured in a 10-pixel radius to ‘infinity’. The 2022 EE(10) values for the filters in this study are shown with black symbols for UVIS1 (crosses) and UVIS2 (open circles). The 2020 EE(10) values adopted by Calamida et al. (2021) are shown in red for UVIS1 (solid) and UVIS2 (dashed), and these differ from the new 2022 values by 0.5% or more for F336W, F200LP, and F850LP. Cyan curves show the 2016 chip-dependent solutions for UVIS1 (solid) and UVIS2 (dashed) which were used to calculate the 2020 inverse sensitivities for all but the bluest and reddest filters, plus F200LP. For comparison, the 2009 inflight EE(10) solution is plotted with a solid navy blue line, while the 2006 pre-launch estimate is plotted with a solid black line.

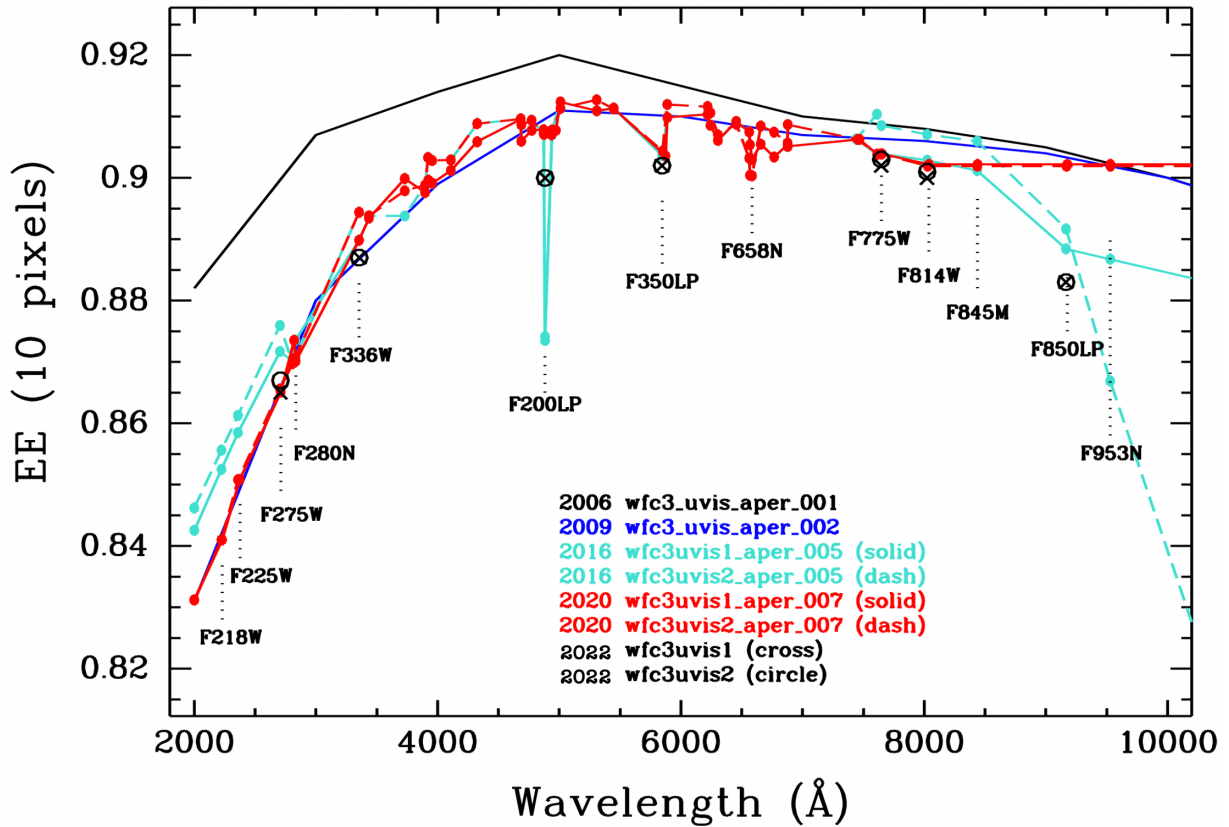


Figure 10: Encircled Energy in a 10-pixel radius, EE(10), as a function of filter pivot wavelength. The filters in this study (2022) are shown as black symbols for UVIS1 (crosses) and UVIS2 (open circles). The EE(10) values from prior studies are overplotted for comparison (see text for details.)

As of 2016, there were not yet enough images from the ‘Photometry Monitor’ to accurately measure the EE at large radii for all filters. Thus, the EE solutions by Deustua et. al (2016) were computed using aperture photometry extending to a radius of 35 pixels (1.4”) and then spliced to the Hartig (2009) model in order to correct the observed count rates to ‘infinity’. Thus the 2016 solutions generally track the 2009 curve, with the largest deviations found for the bluest and reddest UVIS filters. In this analysis, we no longer rely on the 2009 model and compute the EE directly from DRC images with radii extending to 150 pixels (6”).

For UV filters with $\lambda_p < 2800 \text{ \AA}$, the 2016 EE(10) values are $\sim 1\%$ higher than the 2009 value and $\sim 0.5\%$ higher between $3300 < \lambda_p < 4700 \text{ \AA}$. For the reddest filters, $\lambda_p > 8800 \text{ \AA}$, the 2016 EE(10) values are 1% to 2% smaller than the 2009 model. At longer wavelengths, the 2009 EE model likely has larger uncertainties, whereas the 2016 solutions are based on a small number of images compared to the most commonly-used filters. Narrowband filters also have larger uncertainties, particularly F953N where the 2016 solutions were based on just a few images and have EE(10) values which are $\sim 2\%$ lower than the 2009 model for UVIS1 and $\sim 4\%$ lower for UVIS2.

Long pass-filters (F200LP, F350LP, and F850LP) tend to have slightly lower EE(10) values (0.5% or more) compared to UVIS filters with similar pivot wavelengths. The revised F200LP is $\sim 0.8 \pm 0.3\%$ lower than the value adopted by Calamida et al. (2021) who used an interpolated solution from wide UVIS filters similar in wavelength. For this filter, the 2016 EE(10) estimate is more than 2% lower than the 2022 value, but it was based on only four exposures on UVIS2 and had large uncertainties (Deustua et al. 2016). The F350LP EE(10), on the other hand, was based on a much larger set of images for multiple standard stars, and the 2022 values agree more closely with the 2016 solutions to within the measurement uncertainties. For F850LP, Calamida et al. (2021) adopted the EE(10) values from the F814W filter, and these appear to be too large by $\sim 0.9 \pm 0.1\%$. The 2022 values for this filter are closer to the 2016 values where they agree to within $\sim 0.5\%$.

Table 3 lists the 2022 EE(10) values and their estimated errors, along with the EE(10) values from prior studies (2020, 2016, 2009). We computed errors using a combination of Poisson error plus systematic errors resulting from uncertainties in determining the sky background. The maximum Poisson error in the EE(10) ratio was estimated using the formula derived from Taylor (1997):

$$\sigma(EE_{10}) \leq (flux_{150} * \sigma_{10} + flux_{10} * \sigma_{150}) / (flux_{150})^2$$

where $flux_r$ is the flux and σ_r is the error within a circular aperture of radius ‘r’ pixels.

For drizzled images derived from a large number of inflight frames (F275W, F336W, and F814W), the Poisson errors are tiny and range from 0.02% - 0.04%. For drizzled images computed from a smaller set of frames (F200LP, F350LP, F775W, and F850LP+P330E), the Poisson errors range from $\sim 0.10\%$ - 0.15%. For these lower SNR images, we find that the EE curves are more sensitive to small errors in the sky background.

To estimate errors from the background subtraction, we computed an initial sky value from the drizzled image based on the ‘3-sigma clipped mean’ value in an annular ring extending from 160 to 200 pixels in radius. We then adjusted that sky value in small increments ($\pm 0.05 \text{ electrons/pixel}$) and inspected the resulting EE curves. We found that very small changes in the sky for lower SNR

drizzled images can significantly affect the overlap with higher SNR EE curves at radii > 50 pixels, as well as the steepness of the curves at larger radii (e.g. 100 to 150 pixels) as they converge to 1.0. We plot the EE curves for each filter in Figures A1-A7 in the Appendix of this report which are based on the ‘optimized’ sky values.

For F200LP and F350LP (Figures A3 and A4), we increased the sky value for Amp C by ~ 0.1 *electrons/pixel* to bring the lower SNR red curves upwards to more closely match the green curves for Amp A at large radii. This has the effect of changing the EE(10) values by $\sim 0.1\%$. For F850LP (Figure A7), the P330E curves (plus symbols) have Poisson errors which are $\sim 3x$ larger than for GRW+70 (solid circles). The EE(10) values for both CCDs agree to within $\sim 0.1\% - 0.2\%$ for the two different stars, and the EE curves at larger radii generally track one other. However, the lower SNR P330E solutions show small ‘wiggles’ or deviations from the higher SNR GRW+70 solutions

Table 3: UVIS Encircled Energy for seven filters (column 1) measured for each detector amplifier (column 2) using many observations of HST CALSPEC standards (column 5). The pivot wavelength (*Pivot*) and the rms bandwidth (*Width*) are provided in columns 3 and 4 for each filter and correspond to header keywords ‘PHOTPLAM’ & ‘PHOTBW’. The number of FLC images (*N*) and the total exposure time (*Time*) for each drizzled DRC image are listed in columns 6 and 7. The updated 2022 EE(10) values are reported in column 8 with their estimated errors. EE(10) values from prior studies are given in columns 9-11 and correspond to **synphot** aperture correction tables delivered in 2020 (*wfc3uvis1/2_aper_007_syn.fits*), in 2016 (*wfc3uvis1/2_aper_005_syn.fits*), and in 2009 (*wfc3_uvis_aper_002_syn.fits*).

Filter	Amp	Pivot (Å)	Width (Å)	Target	N	Time (sec)	EE(10) 2022	EE(10) 2020	EE(10) 2016	EE(10) 2009
F275W	A	2710	164	GRW	229	1012.2	0.866 ± 0.001	0.865	0.872	0.865
	C				185	938.5	0.867 ± 0.001	0.866	0.876	
F336W	A	3354	158	GRW	139	416.3	0.887 ± 0.001	0.890	0.890	0.886
	C				115	374.1	0.887 ± 0.001	0.894	0.894	
F200LP	A	4972	1742	P330E	12	8.9	0.900 ± 0.003	0.908	0.874	0.910
	C				6	5.0	0.900 ± 0.005	0.908	0.874	
F350LP	A	5874	1490	GD153	28	27.5	0.902 ± 0.001	0.904	0.904	0.910
	C				6	6.0	0.902 ± 0.004	0.904	0.904	
F775W	A	7651	420	GD153	7	60.0	0.902 ± 0.005	0.904	0.904	0.906
	C				8	108.0	0.903 ± 0.003	0.904	0.909	
	A			P330E	12	47.2	0.902 ± 0.002			
	C				10	41.4	0.900 ± 0.003			
F814W	A	8039	667	GRW	117	497.2	0.900 ± 0.001	0.902	0.903	0.906
	C				134	736.0	0.901 ± 0.001	0.902	0.907	
F850LP	A	9176	471	GRW	36	1184.0	0.884 ± 0.001	0.902	0.888	0.904
	C				36	1184.0	0.883 ± 0.001	0.902	0.892	
	A			P330E	12	68.0	0.882 ± 0.004			
	C				8	36.0	0.883 ± 0.006			

especially for Amp C which is slightly lower. We expect that these small deviations will disappear once additional observations are added to the analysis.

For a limiting uncertainty of ~ 0.1 *electron/pixel* in the sky value, the error in the total flux in a 150-pixel aperture radius, $flux_{150}$, varies from $<0.1\%$ to 0.6% , depending on the SNR of the drizzled image. We combine this systematic uncertainty in quadrature with the estimated Poisson errors to produce the errors in Table 3. We note that underestimating the sky background has the effect of producing EE(10) values which are slightly too low, and we speculate that small differences in the ‘optimized’ sky values may be a result of flat field calibration errors which limit the efficacy of the sigma-clipped mean in producing EE curves of the expected shape.

We note that the 2016 EE(10) values in Figure 10 have a larger scatter in UVIS2 compared to UVIS1, with values up to 0.5% larger. This is likely because UVIS2 typically has less than half as many observations as UVIS1 (see Table 6 in Deustua et al. 2016). Additionally, UVIS2 data were primarily acquired after 2013, so systematic errors due to time-dependent changes in the observed count rates will be slightly different for each CCD. While the PSF is somewhat elongated in Amp A compared to Amp C, we believe that differences between UVIS1 and UVIS2 in the 2016 solutions are *not* a result of the slightly different focus. Instead, we suspect that the lower SNR drizzled frames for UVIS2 are more sensitive to small errors in the sky background estimate. In this work, small differences in the EE(10) for the two CCDs are largely removed once the sky background has been adjusted slightly.

5. Conclusions

Both UVIS CCDs show temporal changes in the observed count rates of HST CALSPEC standards throughout WFC3’s lifetime of $\sim 0.1\%$ to 0.2% per year. To avoid introducing systematic errors when combining the images, we rescale the count rates to correct temporal changes *before* computing new EE curves for seven filters.

We compare these results with EE solutions derived in 2009 and 2016. The 2009 inflight EE calibration was derived from saturated images in F275W and F625W to sample the PSF wings with high signal-to-noise out to a radius of $6''$ (150 pixels). These solutions were extended to other UVIS wavelengths using an optical model, with larger uncertainties at long wavelengths. New filter-dependent *and* chip-dependent EE curves were derived in 2016 by combining all inflight monitoring data per filter, computing the EE within an aperture radius of $1.4''$ (35 pixels), and then splicing to the 2009 model in order to correct to $6''$.

Small differences $\sim 0.5\%$ between the two UVIS CCDs in the 2016 EE(10) values are likely a result of systematic errors due to time-dependence in the sensitivity. Additionally, UVIS2 had significantly fewer images, so the EE curves are more sensitive to small errors in estimating the sky background. After correcting for the observed slopes reported by Calamida et al. (2021) and

fine-tuning the sky subtraction, we find that:

- differences in the 2016 UVIS1 and UVIS2 EE(10) for several filters (e.g. F336W, F775W, F814W, F850LP) are now reduced to $\sim 0.1\%$. Similar improvements are expected for other UVIS filters after reprocessing with additional monitoring data and correcting for time-dependence.
- the F275W EE(10) values are $\sim 1.0\%$ lower than the 2016 values for UVIS1 and UVIS2 and within 0.1% of the 2009 EE(10) value to within the 0.1% measurement uncertainty. Because similar changes are expected for other UV filters, Calamida et al. (2021) included a similar correction for F218W and F225W in the 2020 photometric calibration.
- the F336W EE(10) values agree with the 2009 EE(10) value to within the measurement uncertainty of 0.1% . The new values are 0.3% and 0.7% lower than the 2016 values for UVIS1 and UVIS2, respectively.
- the EE(10) values for the F850LP long-pass filter are $\sim 1\%$ lower than the values adopted for the 2020 photometric calibration, which used the F814W filter values. The 2016 EE(10) values were based on ~ 20 images per CCD, and these agree with the current values to within 0.1% . The 2009 value, on the other hand, is $\sim 2\%$ lower and may be a result of uncertainties inherent in the extrapolation of the optical model to long wavelengths.
- for F775W and F850LP, the EE solutions for a white dwarf and a G-type star show no significant differences to within the measurement uncertainties.
- the F200LP EE(10) values adopted for the 2020 photometric calibration were based on an interpolated solution. These are $\sim 1\%$ larger than the values derived from this study.

Because the EE(10) values are used for the UVIS photometric calibration (e.g. to correct the observed countrates in a 10-pixel radius aperture to ‘infinity’ (6 arcsec)), the 2020 solutions by Calamida et al. (2021) will need to be revised to incorporate the updated EE values. For narrowband filters with only a few observations and large uncertainties, additional calibration data will be acquired in the Cycle 29 ‘Photometry Monitor’ (CAL/WFC3 16579), which began in November 2021.

Acknowledgements

We thank Varun Bajaj for helping develop software tools used to align the WCS of the FLC frames and Clare Shanahan for software tools used to calculate aperture photometry. We are grateful to Peter McCullough for reviewing this ISR and for providing helpful feedback to improve its content, especially related to a discussion of the estimated errors. We also thank Joel Green for providing a thorough editorial review.

References

- Anderson, J., Bourque, M., Sahu, K., Sabbi, E., & Viana, A., 2015, “A Study of the Time Variability of the PSF in F606W WFC3/UVIS Images”, Instrument Science Report WFC3 2015-08
- Calamida, A., Mack, J., Medina, J., Shahanan, C., Bajaj, V., and Deustua, S. E., 2021, “New time-dependent WFC3 UVIS inverse sensitivities”, Instrument Science Report WFC3 2021-04
- Deustua, S. E. et al. 2016, “UVIS 2.0 Chip-Dependent Inverse Sensitivity Values”, Instrument Science Report WFC3 2016-03
- Deustua, S. E., Mack, J., Bajaj, V., & Khandrika. H., 2017, “WFC3/UVIS Updated 2017 Chip-Dependent Inverse Sensitivity Values”, Instrument Science Report WFC3 2017-14
- Dressel L., 2013, "Evaluation and Comparison of Deep UVIS PSFs Observed at Three Epochs", Instrument Science Report WFC3 2013-13
- Dressel, L. et al., 2022, “Wide Field Camera 3 Instrument Handbook for Cycle 30, Version 14.0” (Baltimore: STScI)
- Gosmeyer, C. M., Baggett, S., Deustua, S. E., & Hammer, D. M., 2014, “Update on the WFC3/UVIS Stability and Contamination Monitor”, Instrument Science Report WFC3 2014-20
- Hartig, G. 2009, “WFC3 SMOV Programs 11436/8: UVIS On-orbit PSF Evaluation”, Instrument Science Report WFC3 2009-38
- Kalirai, J. et al. 2010, “WFC3 Pixel Area Maps”, Instrument Science Report WFC3 2010-08
- Khandrika, H., Deustua, S. E. , & Mack, J., 2018, “WFC3-UVIS - Temporal and Spatial Variations in Photometry”, Instrument Science Report WFC3 2018-16
- Mack, J., Sabbi, E., & Dahlen, T., 2013, “In-flight Corrections to the WFC3 UVIS Flat Fields” Instrument Science Report WFC3 2013-10
- Mack, J., Dahlen, T., Sabbi, E., Bowers, A. S. 2016, ”UVIS 2.0: Chip-Dependent Flats”, Instrument Science Report WFC3 2016-04
- Sabbi, E. & Bellini, A., 2013, “UVIS PSF Spatial & Temporal Variations”, Instrument Science Report WFC3 2013-11
- Shanahan, C., Gosmeyer, C. M., Baggett, S. 2017, “Update on the WFC3/UVIS Stability and Contamination Monitor”, Instrument Science Report WFC3 2017-15
- Shanahan, C., McCullough, P., Baggett, S. 2017, ”Photometric Repeatability of Scanned Imagery: UVIS”, Instrument Science Report WFC3 2017-21
- Taylor, J. R. (1997) “An Introduction to Error Analysis: The Study of Uncertainties in Physical Measurements”, 2nd Edition, University Science Books, Sausalito

Appendix:

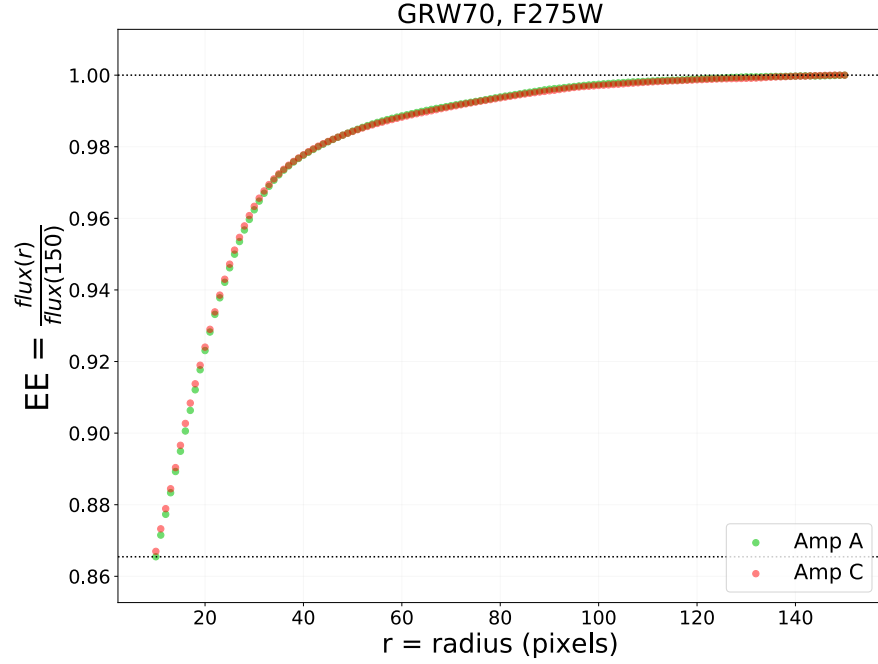


Figure A1: The F275W encircled energy curves, normalized at $r=150$ pixels, based on observations of GRW+70. The drizzled image for Amp A was computed from 229 FLC exposures (1012 seconds total), while the Amp C image was computed from 185 exposures (939 seconds). The dashed line at $r=10$ pixels shows the $EE(10)$ value used for the UVIS photometric calibration.

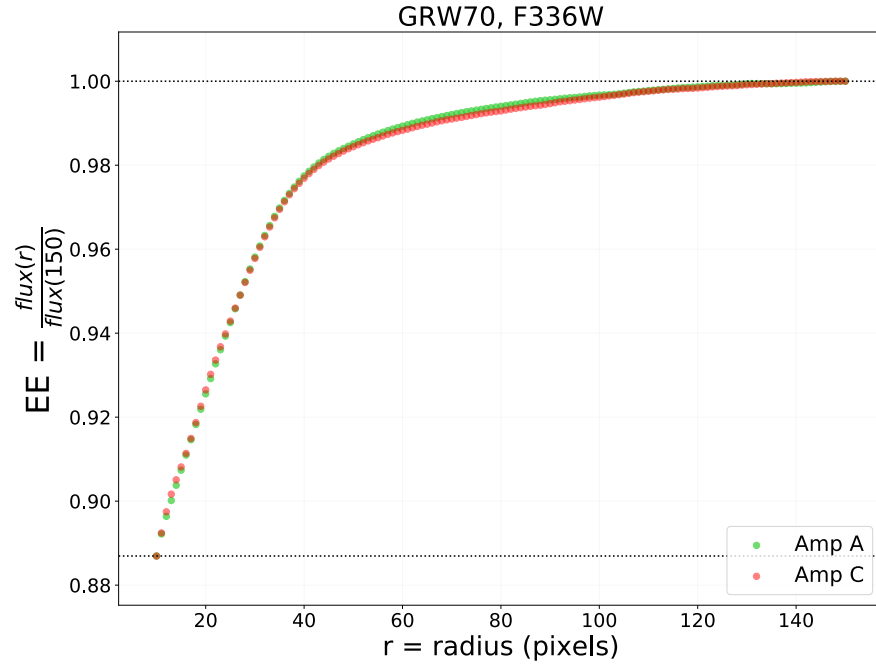


Figure A2: The F336W encircled energy curves from observations of GRW+70. The drizzled image for Amp A was computed from 139 FLC exposures (416 seconds total), while the Amp C image was computed from 115 exposures (374 seconds).

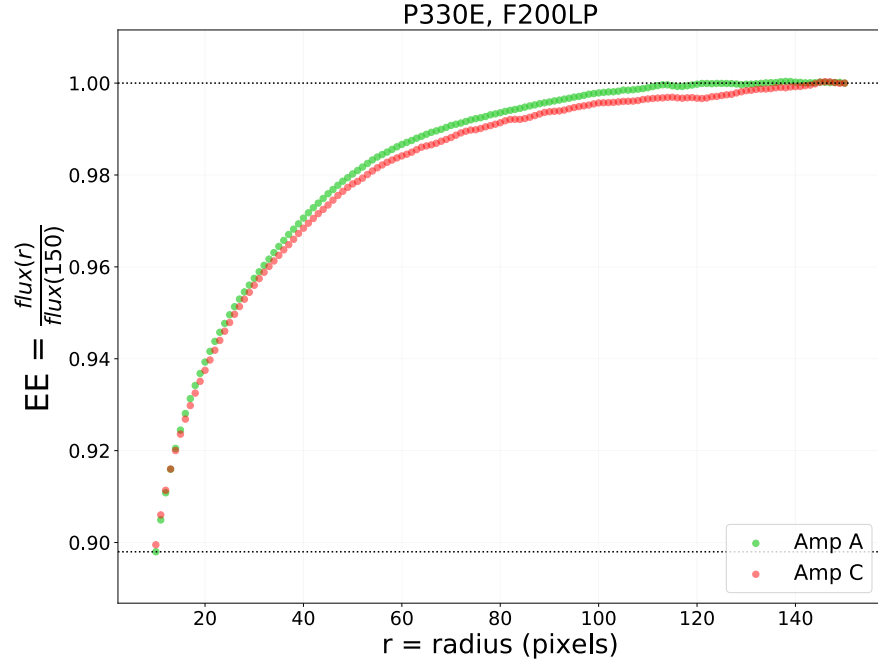


Figure A3: The F200LP encircled energy curves from observations of P330E. The drizzled image for Amp A was computed from 12 FLC exposures (9 seconds total), while the Amp C image was computed from 6 exposures (5 seconds). The lower SNR curve for UVIS2 is expected to more closely match UVIS1 at large radii once additional observations are included for this filter.

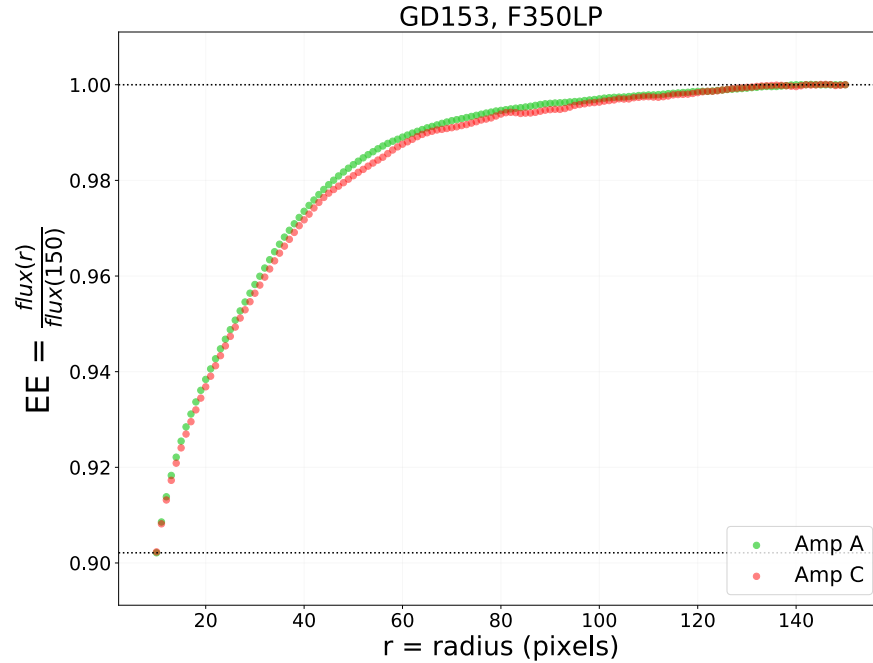


Figure A4: The F350LP encircled energy curves from observations of GD153. The drizzled image for Amp A was computed from 28 FLC exposures (28 seconds total), while the Amp C image was computed from 6 exposures (6 seconds). Despite the significantly lower signal to noise in the combined Amp C data, the two curves agree quite well at radii < 40 pixels.

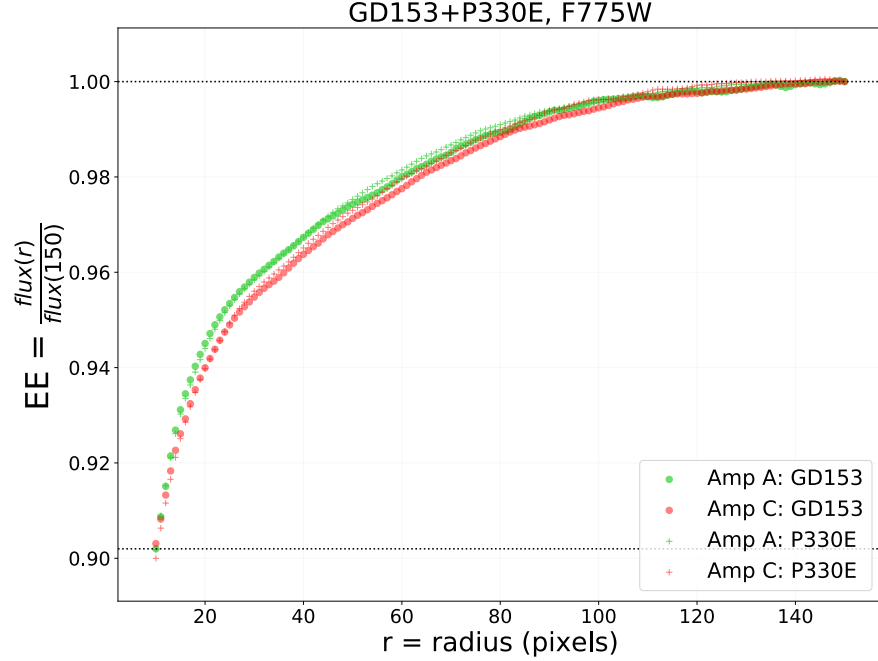


Figure A5: The F775W encircled energy curves from observations of the white dwarf GD153 and the G-type star P330E. The drizzled image of P330E was computed from 12 FLC exposures in Amp A (47 seconds total) and 10 exposures in Amp C (41 seconds). The drizzled image of GD153 was comprised of only 7 exposures in Amp A (60 seconds) and 8 exposures in Amp C (108 seconds). We find no significant differences in the shape of the EE curves due to star color.

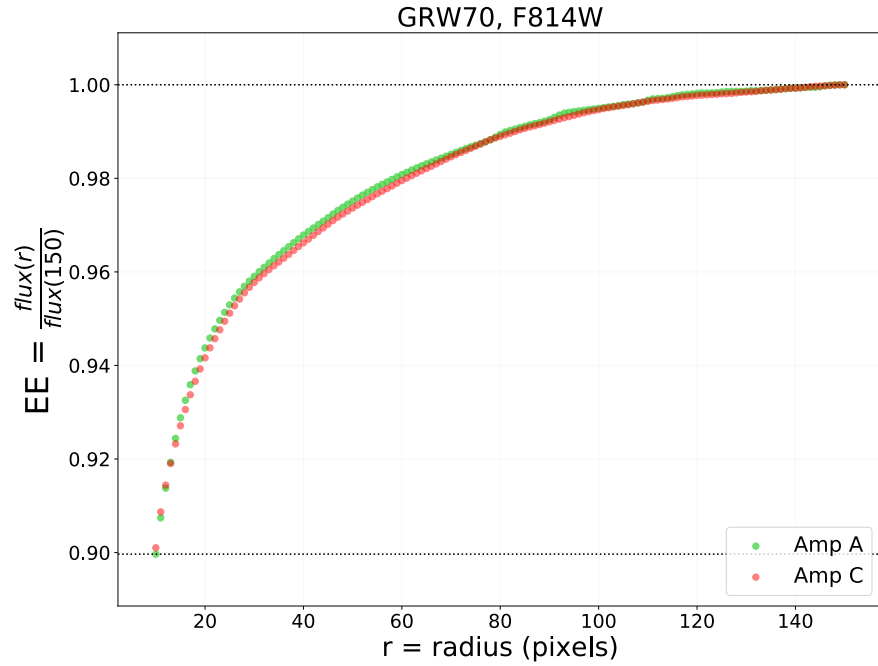


Figure A6: The F814W encircled energy curves from observations of GRW+70. The drizzled image for Amp A was computed from 117 FLC exposures (497 seconds total), while the Amp C image was computed from 134 exposures (736 seconds).

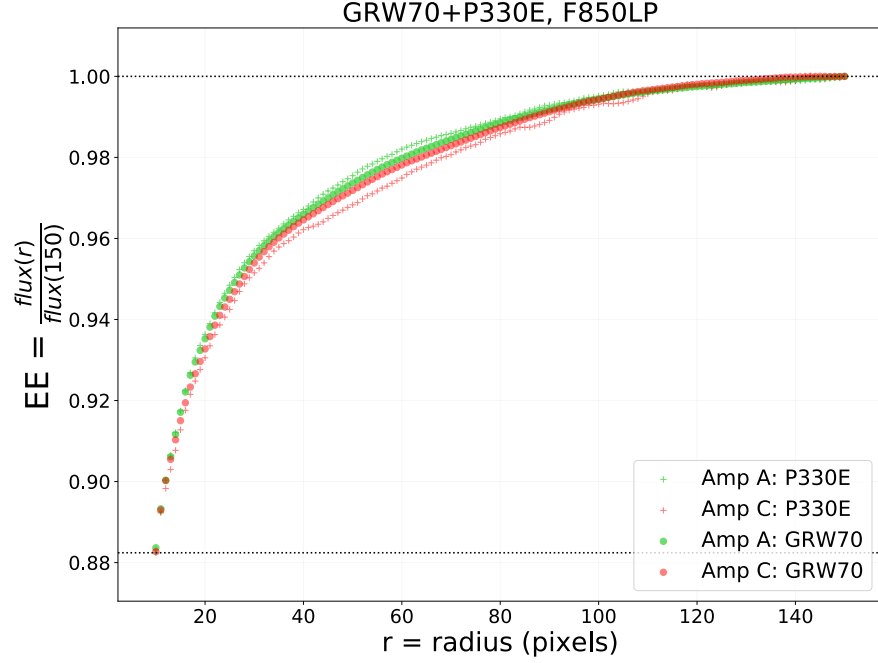


Figure A7: The F850LP encircled energy curves from observations of the white dwarf GRW+70 and the G-type star P330E. The drizzled images of GRW+70 were computed from 36 FLC exposures each in Amps A and C (1184 seconds total per amp). The drizzled images of P330E were derived from only 12 exposures in Amp A (68 seconds) and 8 exposures in Amp C (36 seconds). These are shown as ‘plus’ symbols and have a larger scatter compared to the GRW+70 curve due to their lower SNR and larger errors. As for the F775W filter, we find no significant differences in the shape of the EE curves due to star color.